May 31, 2013

Evolution of Hierarchical Structures in Polyelectrolyte–Micelle Coacervates

Ebru Kizilay
Anthony D. Dinsmore
David A. Hoagland
Lianhong Sun
Paul Dubin, *University of Massachusetts - Amherst*

Soft Matter

RSC Publishing

PAPER

View Article Online
View Journal | View Issue

Cite this: *Soft Matter*, 2013, **9**, 7320

Evolution of hierarchical structures in polyelectrolyte–micelle coacervates

Ebru Kizilay,*[a] Anthony D. Dinsmore,[b] David A. Hoagland,[c] Lianhong Sun[d] and Paul L. Dubin*[a]

Received 26th February 2013
Accepted 30th May 2013

DOI: 10.1039/c3sm50591j

www.rsc.org/softmatter

We investigated the temperature-induced liquid–liquid phase separation (coacervation) of polyelectrolyte (PE)–micelle systems and the structure of the resultant coacervates. Dynamic light scattering, small angle neutron scattering and cryo-transmission electron microscopy (DLS, SANS, Cryo-TEM) were used to examine the evolution of complex structure up to the point of temperature-induced coacervation and beyond. Three diffusional modes, seen in the single phase samples and in the coexisting coacervated supernatant phases were attributed respectively to free micelles, PE–micelle complexes, and aggregates thereof. They corresponded to SANS Guinier region slopes yielding $R_g \sim 4$ nm (micelles) and $R_g \sim 50$ nm (unresolved complexes and aggregates). Cryo-TEM images of coacervates indicated how these subunits are organized within dense and dilute coacervate domains at larger length scales. Taken together, these results are understood to arise from the requirements of overall charge neutralization, and ion-pairing and counterion release during coacervation. We conclude that a polyelectrolyte:micelle system at incipient coacervation with charge stoichiometry ([+]/[−] > 1) donates excess polycations to other complexes in solution. In the coacervate, a similar disproportionation but at different length scales ejects excess polycations and their counterions into dilute domains. In both phases, association and desolvation are driven by counterion release, enhanced chain configurational entropy, and ion-pairing. These enthalpic and entropic forces operating in both phases could explain the structural similarities between soluble aggregates and coacervate dense domains.

Introduction

Complex coacervation is the formation of dense macroion-rich fluids from solutions of oppositely charged polymeric or colloidal macroions, including: (1) oppositely charged polyelectrolytes (PEs);[1–6] (2) PEs with proteins[7–12] and (3) PEs with micelles.[13,14] PE–PE systems have the deepest historical roots and work in that area first demonstrated the formation of soluble complexes at incipient coacervation.[1] While PE–PE systems form a dense, homogeneous fluid in which the properties of individual macroions are lost, the structure and function of colloids such as proteins and micelles[15] appear to be retained in PE–colloid coacervates.[16] However, the ability to modulate colloid functionality depends on controlling coacervate mesostructures. PE–protein coacervates, for example, unlike PE–PE coacervates, have complex internal structures, structurally heterogeneous on many length scales.[17,18]

Polyelectrolyte–micelle coacervates exhibit equilibrium structures, formed by short-range attraction and long-range repulsion, with unique temperature dependence.[19] While these hierarchal systems are organized from the nm to micron scale, the way in which dynamic and structural properties change as a consequence of the phase transition is not clear. Examination of polyelectrolyte–micelle systems allows us to understand fundamental principles in complex coacervation, particularly with respect to the evolution of the dense phase.

In typical complex coacervation, oppositely charged macroions combine to release counterions and water,[8,20,21] but this process is frustrated by geometric constraints and a lack of charge complementarity, resulting in significant retention of counterions and solvent. For oppositely charged systems, coulombic[22] and entropic effects[23] fully overcome the usual incompatibility of unlike components to form soluble complexes and aggregates leading to a dense, homogeneous fluid.[24] Soluble inter-macroionic complexes, established as precursors of coacervation[6,19] are in equilibrium with their own components, but whether these complexes remain present in phase-separated samples remains an open question.

Mixing of aqueous solutions of polycations and polyanions (the PE–PE case) leads to formation of soluble aggregates that form a separate phase with enhanced polymer concentration.

[a]*Department of Chemistry, University of Massachusetts Amherst, MA 01003, USA. E-mail: ekizilay@chem.umass.edu; dubin@chem.umass.edu*

[b]*Department of Physics, University of Massachusetts Amherst, MA 01003, USA*

[c]*Department of Polymer Science and Engineering, University of Massachusetts Amherst, MA 01003, USA*

[d]*School of Life Sciences, University of Science and Technology of China, Hefei, Anhui 230027, People's Republic of China*

While the absence of soluble aggregates of any type, as proposed by Overbeek *et al.*,[25] is still supported in some studies,[26] most experiment confirms the view of coacervation as a two-step process, as described by Veis and Aranyi.[1] In this model, electrostatic interactions lead to spontaneous formation of soluble complexes of oppositely charged chains, which rearrange to form a macroscopic concentrated coacervate phase. In the Veis–Aranyi model, the equilibrium supernatant contains only excess polyions, but the presence of higher molecular weight aggregates composed of soluble complexes at incipient coacervation was confirmed more recently by Veis.[24] Such electrically neutral aggregates reach coacervation by one of two[37] pathways: (1) PEs are randomly mixed upon phase separation or (2) aggregates at least in some form remain in both coacervate phase and supernatant phase. While both these paths can support the existence of aggregates at incipient coacervation, they differ with regard to the presence or absence of aggregates in the coacervate. These alternatives as expressed for both PE–PE and PE–colloid coacervation,[20] but important distinctions remain.

Complex coacervation in colloid–PE systems differs from that in PE–PE systems owing to two factors: the typically greater polydispersity in the latter, and the fundamental asymmetry of the former. MW and chemical polydispersity of most PE's studied leads to heterogeneity in the PE–PE systems which broadens all observed transitions including coacervation. Fundamental behavior as a true liquid–liquid phase transition is then often masked. This broadening also complicates the identification of soluble complexes (one polymer chain complexed with *ca.* 7–55 proteins[27] or *ca.* 15–70 mixed micelles[28]). These intrapolymer or "primary" complexes and aggregates thereof, well-characterized in systems of PE and proteins[29] and PE and mixed micelles,[30] have been established as antecedents of coacervates. Second, such polyelectrolyte–colloid systems have an inherent asymmetry different from PE–PE coacervates inasmuch as the difficulty of commingling ionic groups limits random mixing. PE–PE systems form a dense, homogeneous fluid in which component properties are lost;[24] on the other hand, when one of the macroions is a protein, its structure and properties appear to be retained.[16] The integrity of the colloidal component is particularly central to applications of PE–protein coacervates, and to their structural characterization[45] which focuses to large extent on the dynamics and arrangement of the colloidal component.

PE–protein coacervates, unlike PE–PE coacervates, have complex internal structures, structurally heterogeneous on many length scales, which affect coacervate dynamics.[3,31–33] A variety of meso-scale structures of polyelectrolyte–protein coacervates are indicated by multiple diffusivities seen by dynamic light scattering[34] and by fluorescence recovery after photobleaching (FRAP)[35] which probes longer length/time scales. The fast diffusive mode detected by dynamic light scattering (DLS) is only one order of magnitude slower than that of dilute protein, which demonstrates that microheterogeneity allows the nearly free diffusion of proteins in certain domains despite the very viscous nature of the bulk coacervate. An additional slow non-diffusive mode revealed by DLS was correlated with the relaxation time (lifetime) of the dense domains.[34] Kayitmazer and coworkers studied the structure of coacervates prepared with BSA/PDADMAC and BSA/chitosan, two polycations of equal linear charge density but very different persistence lengths by combining rheology and SANS.[34] The connectivity and size of the protein-rich domains in the coacervate depended on the protein charge. Rheology revealed the presence of the equilibrium network in that the elastic behavior was reconstituted after breakage with extensive shear.[36] Contrast matching SANS studies of lysozyme and polystyrenesulfonate PSS mixtures with excess PSS[37] revealed the presence of mesoscopic (*ca.* 40–100 nm) structures, which were interpreted as arising from short-range attractions that stabilize Lys/PSS neutral cores, and long-range repulsions between primary complexes that determine overall length scales.[38] This segregation of components into mesophase domains is dramatically different from the molecular random mixing proposed for PE–PE coacervates.

For PE–colloid coacervates, a balance of short-range attraction and long-range repulsion (SALR)[39] leads to formation of aggregates by attraction among primary soluble complexes, driven by the elimination of transient regions of low macroion charge compensation but limited by charge accumulation. Enhanced charge compensation is accompanied by the release of counterions, generally recognized as a dominant driving force in complex coacervation,[18,40] further substantiated by calorimetric measurements for PE–micelle systems.[41] Such equilibrium measurements require modulation of the PE–colloid interaction, readily achieved in the PE–micelle through the use of mixed nonionic–ionic micelles whose attenuated surface charge densities allow for complexation without uncontrolled phase separation. The low cmc of these mixed micelles renders the effect of monomeric surfactant negligible, and provides control of the PE–micelle interaction via the mole fraction of ionic surfactant Y.[42] After the combination of electrostatic attractive forces and counterion release have lead to a sufficient number of aggregates, the size of larger species forming from them is limited by charge accumulation. Uniquely, the clusters observed in the PE–micelle system are subject to disproportionation manifested as splitting into respectively smaller and larger particles, and accounted for by a drive towards charge neutrality itself promoted by subsequent coacervation.[43] As a result, phase separation of coacervation could establish a new equilibrium between supernatant and coacervate leading to alterations in the clusters originally in the one-phase system. When viewed by the classical colloid model (2-component binodal),[44] this alteration is simply a change in aggregate concentration. But if phase separation includes aggregate rearrangement, the classical model would have to be modified to account for the *compositional* difference between dilute and concentrated phases (here supernatant and coacervate).[45] Even though clusters within these two phases are of different composition, they might be of comparable size if a similar combination of short-range attraction and long-range repulsion forces is present in both supernatant and coacervate.

Polyelectrolyte–micelle systems allow us to investigate the integrity of structural units in soluble complexes *vs.* their reassembly in modified forms under the influence of the parallel

energetic and entropic factors that drive phase separation. A unique aspect of the PE–micelle system is an exquisite sensitivity to temperature, for both the coacervate[46,47] and the one-phase solution.[19] True liquid–liquid temperature-induced transitions (T_Φ) are observed when surfactant polydispersity is minimized. The coacervate itself exhibits a second transition at $T'_\Phi > \mathbf{T}_\Phi$ leading to a new coacervate and supernatant,[10,47] but the relationship between these two transitions has not been previously examined. Regardless of this issue, the unique temperature-sensitivity of the PE–micelle system greatly facilitates *in situ* study of complexation and coacervation. Following in this way the evolution of complex structure up to the point of temperature-induced incipient coacervation and beyond offers further insight into the correlation between these two processes and their consequent structures. The consequences of these effects for coacervate structure, and their tendency to continue when the coacervate itself is heated, are not yet fully known.

Polyelectrolyte–micelle and polyelectrolyte–protein systems are closely related in their sensitivity to colloid surface charge density, and the role of salt in screening long-range intermacromolecular electrostatic interactions. The cooperative binding of PE segments to the colloidal particle results in critical conditions for binding (Y_c [30] and pH_c [29]) closely analogous to theoretical treatments of PE–colloid adsorption.[48,49] The PE–micelle system thus differs from those PE–surfactant mixtures amenable to rigorous thermodynamic treatments through phase diagrams in which PE, (monomeric) surfactant, and salt are considered as well-defined components of a ternary system.[50,51] The elimination of simple counterions in the PE–surfactant mixtures (forming complex salts that consist of surfactants with polymeric counterions in a 1 : 1 charge stoichiometry), enables these systems to be described in truly ternary phase diagrams. Here, the two surfactants form a single colloid particle, and the role of salt is contribution to the ion atmosphere. The corresponding model successfully explains the interrelationship of mixed micelle composition (Y), PE linear charge density and ionic strength, at critical conditions corresponding to the onset of complex formation.[19,30] Additional sets of conditions, defining the transition from soluble complexes to coacervate, can be represented as phase boundaries, differentiated from the phase diagrams adopted for the truly ternary systems mentioned above.[50,51]

The purpose of the present work is to examine the degree to which mesophase domains within the PE–micelle coacervate phase retain structural features of their soluble aggregate precursors. We follow the evolution of complex structure up to the point of temperature-induced coacervation and beyond. We compare our results to two models appropriate for PE–colloid systems. The first model views the soluble aggregates as colloid particles susceptible to a gas–liquid phase separation process[52] without structural rearrangements at the <100 nm length scale. In the second model, the phase change is driven by such rearrangements and a new structural length scale appears in the coacervate owing to the same mechanisms that led to aggregate formation in the single phase systems.

To address these questions, we use a system in which a strong polycation, poly (dimethyldiallylammonium chloride) (PDADMAC) ($M_w/M_n = 1.1$), binds mixed micelles of the anionic surfactant sodium dodecyl sulfate (SDS) and the nonionic surfactant Triton X-100 (TX100). Because of the very low cmc of SDS-TX100 mixed micelles (*ca.* 0.2 mM),[42] SDS is incorporated into TX100 micelles instead of interacting directly with PDADMAC in which case precipitation could occur. Instead, the interaction with polymer is modulated by the mixed micelle surface charge density. The micelle surface potential is then controlled by the mole fraction of SDS in the mixed micelles (Y) and the ionic strength I.[30] The value of Y controls only the micelle charge; therefore the molar concentration of polymer has no effect on Y. The fundamental significance of Y (the experimental parameter corresponding to micelle charge) is evident from the way in which Y_c *vs.* I corresponds to theory. When the ratio of total micelle charge to total polycation charge approaches unity the system tends to phase separate in a manner similar to the behavior of other oppositely charged macroion pairs. Advantages of the PDADMAC/SDS-TX100 system over other coacervating polyelectrolyte–colloid systems are (1) the structural simplicity of the polyelectrolyte (*e.g.* lacking hydrophobic and pH-dependent elements), and the low heterogeneity of the system which reveals the true sharpness of the phase change, often obscured by system polydispersity;[53] and (2) the ability to control the range in which the coacervate phase is stable by adjusting Y and I, and appropriately choosing polymer molecular weight M_w, concentration C_P, and polymer : micelle stoichiometry w.[30] These values are chosen according to prior work that defined the regimes of soluble complexes, coacervates or precipitates. Since temperature T is the critical variable in this work, we chose the values of $Y = 0.35$, $I = 0.40$ and $w = 0.15$ at which $T_\Phi = 24$ °C allowing for convenient manipulation of pre- and post-coacervation states. Since the bulk charge stoichiometry ([+]/[−]) at $Y = 0.35$ is 1.7, the system comprises excess polycation ($Y = 0.44$ corresponds to [+]/[−] = 1). We explore the structure of pre-coacervate and coacervate phases at fixed Y, I and w, and at varying T by DLS, SANS and Cryo-TEM. The last method serves to support the model-dependent conclusions from SANS.[34]

Experimental section

Materials

Poly(diallyldimethylammonium chloride) (PDADMAC) was prepared by free radical aqueous polymerization of diallylmethylammonium chloride, and characterized by light scattering and osmometry.[54] Its weight and number-average molecular weight (from membrane osmometry) were determined as $M_w = 5.2 \times 10^5$ and $M_n = 4.6 \times 10^5$. Triton X-100 (TX100) and sodium dodecyl sulfate (SDS, purity >99%) were purchased from Aldrich, and NaCl was from Fisher. All were used without further purification. Milli-Q water and/or D_2O were used in all experiments.

Coacervate preparation

60 mM SDS in 0.40 M NaCl was added with continuous stirring to solution of 3 g L^{-1} PDADMAC (below overlap concentration

~10 g L^{-1}) in 20 mM TX100 (also in 0.4 M NaCl) to bring the mole fraction of SDS (Y) to 0.35. Y is defined as:

$$Y = \frac{[\mathrm{SDS}]}{[\mathrm{SDS}] + [\mathrm{TX100}]} \quad (1)$$

The resultant suspensions were stirred for 15 min and centrifuged for at least 2 h at 3750 rpm at 24 °C to yield a dilute ("supernatant") and a dense phase ("coacervate") (both optically clear).

Turbidimetric measurements

Turbidity, reported as –log(τ) was measured using a Brinkmann PC 800 colorimeter ($\lambda = 450$ nm) equipped with a 1.0 cm path length fiber-optics probe. Turbidity values were recorded as function of temperature with the sample continuously stirred during the heating. All measured values were corrected by subtracting the turbidity of a polymer-free blank. Duplicate titrations gave reproducible results.

Dynamic light scattering (DLS)

DLS was conducted with a Brookhaven Instruments BI-200SM goniometer equipped with a PCI BI-9000AT digital correlator, a temperature controller, and a solid-state laser (model 25-LHP-928–249, $\lambda = 633$ nm). Measurements were usually carried out at 12–21 °C at scattering angle of 90°, with additional angle studies.

The samples were stirred for at least 2 h and filtered with Whatman (0.2 mm) filters prior to measurements. The correlation functions of the scattering data were analyzed *via* non-negative least squares fit (NNLS)[55] and then used to determine diffusion coefficients (D). D can be converted into hydrodynamic radii using the Stokes–Einstein equation:

$$R_{\mathrm{H}} = \frac{kT}{6\pi\eta D} \quad (2)$$

where k is the Boltzmann constant, T the absolute temperature, and η is the solvent viscosity, here taken as that of water. Measurements were done in multiple. It is remarkable that the DLS correlation functions as well as the corresponding fitting parameters are very stable in time.

SANS measurements

Scattering experiments were carried out on the NG3 spectrometer at the National Institute of Standards and Technology (NIST) in Gaithersburg, MD. SANS spectra $I(q)$ were measured as a function of the scattering vector $q = (4\pi/\lambda)\sin\theta$. Here λ is the neutron wavelength, ($\lambda = 6$ Å) and 2θ the scattering angle. Samples were held at a fixed temperature in the range of 18–25 °C in 1 or 2 mm quartz cells. The raw data were normalized; radially averaged, and masked using the standard software provided by NIST, and then put on an absolute scale by measuring the scattering of a standard provided by NIST. Scattering from an empty cell and background (90% D_2O and 10% H_2O) scattering were subtracted for all spectra. By subtracting this incoherent background from the scattering of the sample the coherently scattered intensity was calculated.

SANS analysis

SANS data[56] was best fitted by the two-level Beaucage model[57] characterized by three fitting parameters: a Guinier scaling factor G, a radius of gyration R_g and a Porod exponent P. The scattering intensity is given by

$$I(q) = \sum_{i=1}^{2}\left[G_i \exp\left(-q^2 {R_{g,i}}^2/3\right) + \frac{B_i\left[\mathrm{erf}\left(qR_{g,i}/\sqrt{6}\right)\right]^{3P_i}}{q^{P_i}}\right] \quad (3)$$

A radius of gyration and a power law slope describes each structural level. Two R_g and two Porod exponent values were obtained at each length scale.

Cryogenic transmission electron microscopy (Cryo-TEM)

Cryo-TEM was performed on a TX100/SDS–PDADMAC coacervate. A controlled environment chamber was used to maintain the sample temperature and suppress any evaporation. A few microliters of the fluid sample are taken by pipette and set onto a specially prepared holey carbon grid. The sample was then plunged into a cryogen reservoir, typically liquid ethane close to its melting point. Contact with the cryogen induces rapid solidification of the sample at 16–18 °C, causing the water in the solution to vitrify rather than crystallize. This rapid vitrification preserves all of the microstructures in their original state. The microscope grid was then transferred under positive dry nitrogen pressure to a cold stage for subsequent phase contrast imaging in the electron microscope.

Results

Soluble complexes and single-phase samples

Fig. 1 shows turbidity as a function of temperature. In separate measurements, we also measured the turbidity values during cooling. The absence of hysteresis verified that the sample reaches a steady state at each temperature before the turbidity is measured. The lines of Fig. 1 show the determination of the phase separation temperature, here $T_\Phi \sim 20$ °C. The initial gradual increase in τ is ascribed to progressive formation of interpolymer soluble complexes, involving multiple polymer chains.[19] In the vicinity of T_Φ the small increase in turbidity arises from the formation of interpolymer complexes, and at $T > T_\Phi$, the abrupt increase in turbidity indicates formation of a suspension of microscopic coacervate droplets in a continuous dilute phase. That these droplets are actually themselves monophasic is demonstrated by the fact that they coalesce to form an optically clear dense phase upon centrifugation at $T > T_\Phi = 20 \pm 1$ °C (4700 rpm, 2 hours), resulting in optically clear dense and dilute phases with a well-defined boundary.

We performed DLS measurements in the temperature range 16 °C < T < 20 °C to obtain the size distributions shown in Fig. 2. While measurements were typically performed ~20 minutes after temperature adjustment, results were not particularly sensitive to time as verified by reproducibility of dynamic light scattering (DLS) spectra after two hours. This stability over time is consistent with previous observations involving DLS time intervals as small as 5 minutes[43] and also with substantial evidence from

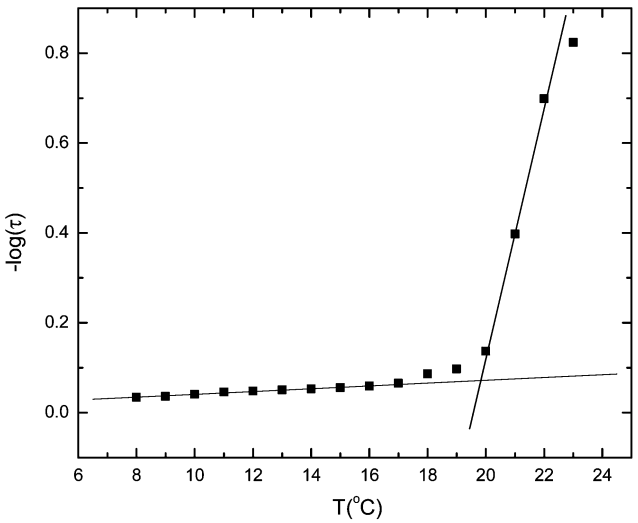

Fig. 1 Turbidity as a function of temperature for the PDADMAC/TX100-SDS solution.

many techniques attesting to the steady-state equilibrium nature of the soluble complex.[46] For $T > T_\Phi$, the turbidity precludes DLS measurements. For $T < T_\Phi$, the system displays modes at $D = 2.1 \times 10^{-7}$ cm^2 s^{-1}, 1.2×10^{-7} cm^2 s^{-1}, 1.3–1.5 $\times 10^{-8}$ cm^2 s^{-1}, *i.e.* $R_H = 7 \pm 1$; 17 ± 2; and 95–125 nm. The last two modes are attributed respectively to intrapolymer soluble complexes and aggregates thereof. The free micelles contribute the fastest decay mode, and a relatively weak signal that is suppressed at the lowest angles by the scattering from complexes.[19,43] Sizes of individual micelles ($R_H \sim 7 \pm 2$ nm) and polymers ($R_H \sim 15 \pm 2$ nm) were determined in our previous studies.[19,30]

Coacervates

Turbidity and DLS. To study the structure of the coacervate phase at $T > T_\Phi$, the sample was initially held at $T < T_\Phi$ (*e.g.* 10 °C) for two hours before centrifuging at 22 °C for two hours. The coacervate phase was extracted from the bottom and the supernatant was extracted from the top. The transparent and viscous coacervate fluid shows an increase in turbidity with temperature (Fig. 3) remarkably similar to the behavior of the starting solution (Fig. 1). Evidence that T'_Φ also marks a phase transition comes from visual observation,[19] rheology[46] and from the appearance of shear lines.[19,47] The gradual increase of turbidity as T approaches T'_Φ indicates the formation of larger species or structures within the coacervate.

To probe the dynamics and sizes of these species, we obtained DLS spectra of the coacervate at temperatures ranging from 12–21 °C and analyzed them *via* NNLS. As shown in Fig. 4 and 6, they consistently and reproducibly exhibit three decay modes. In order to investigate the origins of the coacervate slow modes, their dependence on the scattering angle θ from 20° to 150° was measured and the corresponding decay rates Γ are plotted as a function of scattering wave vector q at 12 °C < T < 21 °C ($q = 0.000347$ corresponds to $\theta = 90°$). Similar results are shown for the fast and intermediate modes, which show little temperature dependence. The linearity of Γ *vs.* q^2 seen in Fig. 4a confirms the diffusional nature of fast and intermediate mode. In contrast, the slow mode exhibits two different slopes (Fig. 4b). These aggregates get larger close to T'_Φ as supported by the smaller slope at 21 °C. At large q values, q-independent regions exhibit decay rates that get smaller as the temperature increases. We plot $\Gamma/(q^3 k_B T/\eta)$ *vs.* $R_g q$ to help understand the nonlinear q-dependence since the scaling of Γ with q^3 is

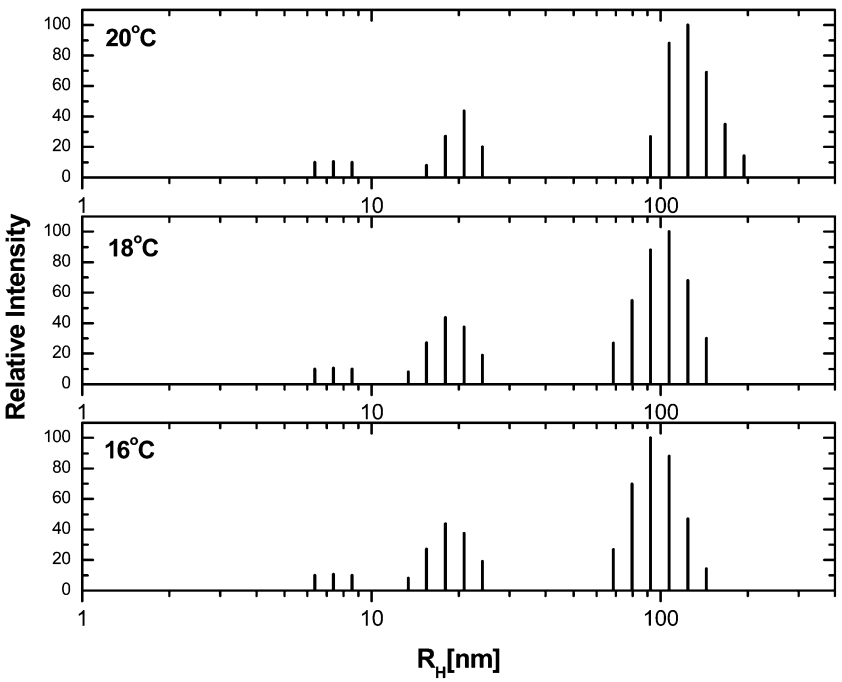

Fig. 2 Relative intensity *vs.* hydrodynamic radius for single-phase PDADMAC/TX100-SDS solution of Fig. 1 at 16 °C, 18 °C and 20 °C.

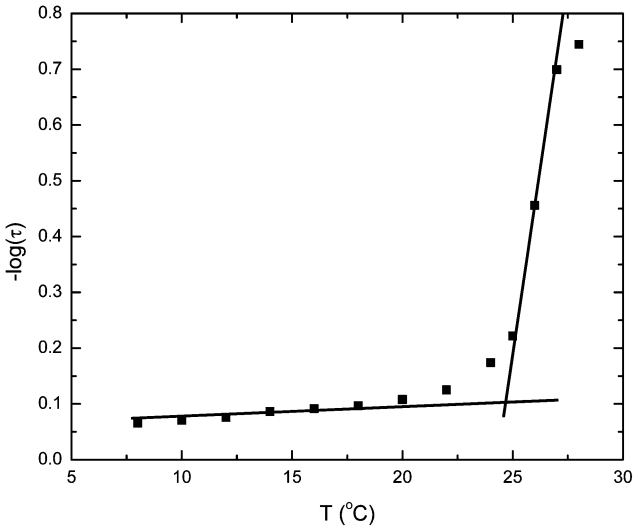

Fig. 3 Turbidity as a function of temperature for the coacervate phase extracted at 22 °C from the PDADMAC/TX100-SDS solution of Fig. 2.

observed in the case of internal motions of chains[58] (Fig. 5). As $R_g q$ increases, $\Gamma/(q^3 k_B T/\eta)$ gradually decreases and approaches a plateau. This scaling of Γ with q^3 is also observed in a microgel particle that exhibits q independent behavior due to the internal motions.[59] Overall, the intermediate species show a small decrease in D close to T_Φ', the slow mode shows a large decrease in D, apparently parallel to the intermediate mode but very prominent near T_Φ'.

The species with $D = 2.1 \times 10^{-7}$ cm^2 s^{-1} (obtained from the slope of the mean decay rate Γ *versus* q^2 plot) indistinguishable from the fast mode values obtained in the one-phase system (Fig. 2) and can be attributed to free micelles with a diffusion coefficient only 15% less than that of micelles in an aqueous medium.[46] If we assume that the background viscosity is the same as that of water (which is nearly the case for the micelles), we can then obtain hydrodynamic radii for each mode. The slope of the intermediate mode is obtained as $D = 1.2 \times 10^{-7}$ cm^2 s^{-1}, corresponding to size $R_H = 18 \pm 2$ nm, very close to the value of species seen prior to coacervation in Fig. 2. While the apparent size of the slow mode in the coacervate $R_H = 117$ nm ($D = 1.4 \times 10^{-8}$ cm^2 s^{-1}) is similar to the value of the slow mode in the one-phase system ($R_H = 95$–125 nm) attributed to aggregates of intrapolymer complexes, aggregate size evolves to $R_H = 240$ nm ($D = 0.7 \times 10^{-8}$ cm^2 s^{-1}) close to T_Φ. These hydrodynamic sizes calculated by using water as the background viscosity are very close to sizes of the objects present in the one-phase system which has a bulk viscosity

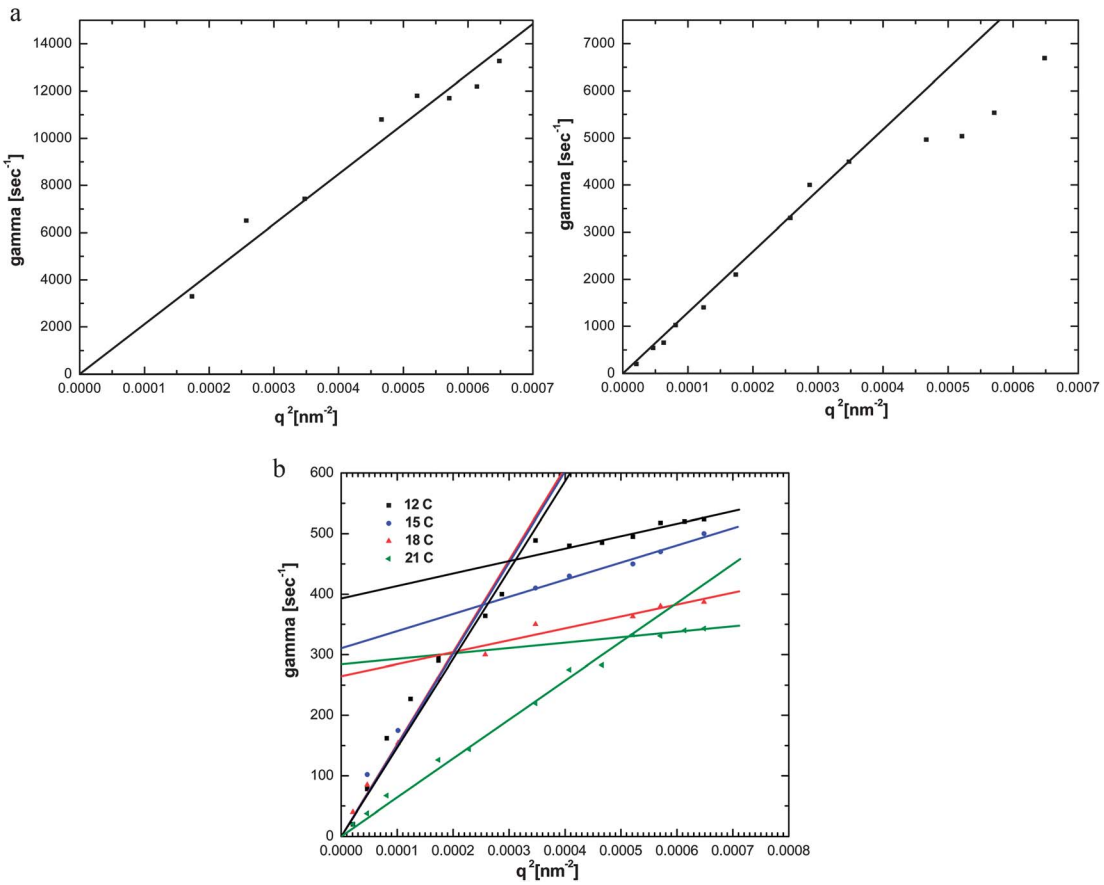

Fig. 4 (a) The mean decay rate (Γ) *versus* q^2 for fast mode (left graph) and intermediate mode (right graph) of coacervate phase at 15 °C. The disappearance of the fast mode at $\theta < 40°$ is due to the expanded contribution of large particles. (b) The mean decay rate (Γ) *versus* q^2 for slow mode of the coacervate phase.

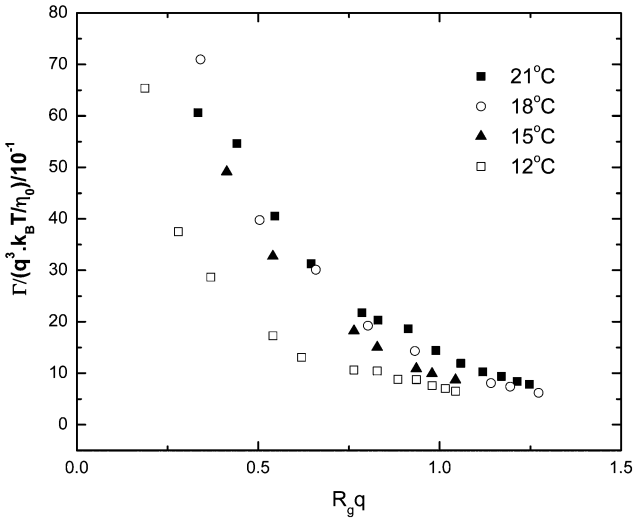

Fig. 5 $\Gamma/(q^3k_BT/\eta)$ *vs.* R_gq for slow mode of the coacervate phase. R_g values obtained from SANS are used.

almost same as water. This implies that these modes experience a local viscosity smaller than the macroscopic or bulk viscosity of the medium. Since the bulk viscosity of the coacervates is about 1000 times larger than water, complexes and aggregates probably move in an unobstructed way in a region with much lower viscosity.

The temperature dependence of all three modes is shown (Fig. 6). Micelle size does not show any temperature dependence; in contrast R_H progresses slightly from 18 nm to 28 nm as (from 9–1 °C below T_Φ'). As supported by the mean decay rate (Γ) *vs.* q^2 plot for slow mode, temperature has a large effect on the size of the large aggregates at a temperature very close to T_Φ', while at lower temperatures (from 9–4 °C below T_Φ') the size of the slow mode increases slightly from 117 nm to 135 nm.

The supernatant also exhibits three decay modes (Fig. 7). We investigated these species as a function of temperature ranging from 15 °C to 20 °C. DLS fast, intermediate and slow modes are attributed to free micelles, soluble complexes and soluble aggregates, respectively. Free micelles (R_H = 6.5–8 nm) do not show any temperature dependence; however R_H of the soluble complexes slightly increases from 18 nm to 22 nm. The apparent size of the slow mode (R_H = 80–105 nm) in the supernatant is similar to the value of the slow mode in the one-phase system.

SANS

SANS was used to further characterize the structures of species in the coacervate as a function of temperature. The Beaucage model was employed to fit the data for the coacervate at different temperatures, and the fitting parameters are given in Table 1. The size of soluble aggregates varies non-monotonically with temperature with a weak maximum at 23 °C, while R_g values for the micelles are between 3 and 4 nm. Surface fractals have Porod exponents between 3 and 4, while mass fractals that correspond to Porod exponents between 1 and 3 indicate particles without a distinct surface. The best-fit Porod exponent that increases from 2.0 to 2.2 corresponds to the mass fractal of the complexes and/or aggregates, while the Porod exponent of 4.8 corresponds to surface scattering, which might be an indication of spherical micelles. Columns 2 to 5 in Table 1 will be further discussed with the coacervate Cryo-TEM image (Fig. 9).

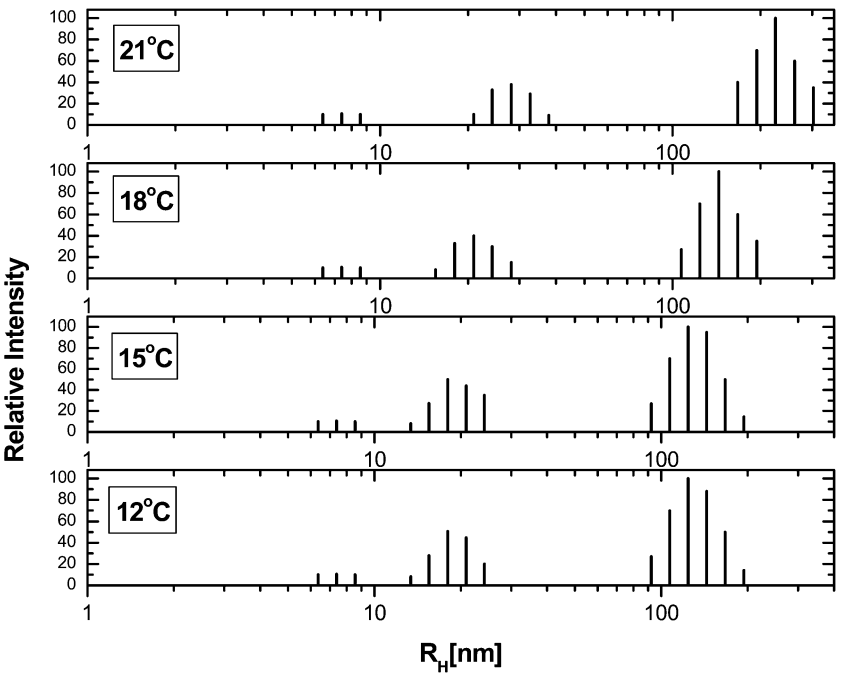

Fig. 6 Relative intensity *vs.* hydrodynamic radius for coacervate of PDADMAC/TX100-SDS from 12 °C to 21 °C.

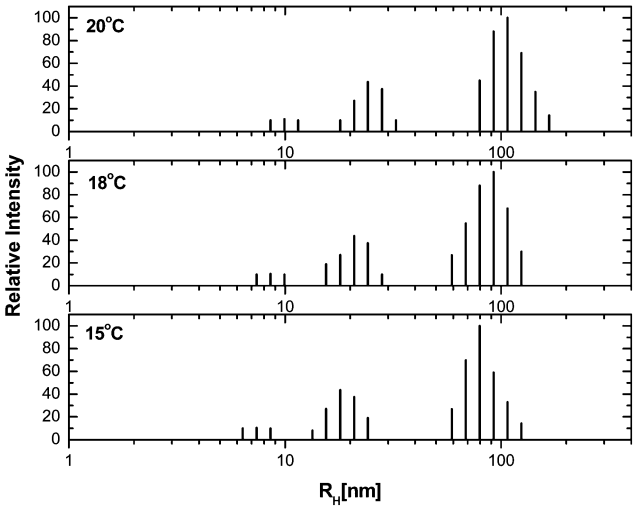

Fig. 7 Relative intensity *vs.* hydrodynamic radius for supernatant of PDADMAC/TX100-SDS from 15 °C to 20 °C.

Cryo-TEM

The Cryo-TEM image in Fig. 9 is seen to be composed of dense 200 nm clusters which are interconnected to form extended assemblies with dimensions on the order of one μm. Free micelles appear as isolated 10 nm dots. The possible retention within the coacervate of structural features of aggregates at $T < T_\Phi$ (prior to phase separation) is observed. Previous studies showed that phase state of the system depended on the magnitude of the difference between the Cryo-TEM vitrification temperature (T_{vitr}) and the second phase separation temperature (T'_Φ).[47] If this difference is large, the system will be far from incipient phase separation, and therefore difficult to compare to the one-phase system at incipient coacervation. Consequently, the coacervate was prepared so as to have small difference between the Cryo-TEM vitrification temperature (T_{vitr}) and T'_Φ. At similar temperatures we could examine the structure of the coacervate prior to its phase separation at T'_Φ.

Discussion

Approach to coacervation

Fig. 1 and 2 together indicate formation of progressively larger soluble aggregates from primary (intrapolymer) complexes as $T \rightarrow T_\Phi$, both in equilibrium with free micelles. The depth of entry into the coacervate region at any given temperature increases with decreasing T_Φ, which displays a symmetrical minimum at $Y = 0.38$,[19] a point designated at Y^*, since it also corresponds to (1) the formation of charge neutral complexes,[30] and (2) maxima in $\tau(Y)$.[19] It does not however correspond to [+]/[−] = 1, which corresponds to $Y = 0.44$. The fact that many features at $Y = 0.38$ seem consistent with charge neutral complexes, even though [+]/[−] = 1.37 signifies that the composition of complexes need not be the bulk composition.[60] Thus, the formation of aggregates from intrapolymer complexes suggests ways of achieving neutrality on the microscopic scale. Indeed DLS modes with were seen to exhibit splitting of 50–100 nm aggregates into larger and smaller species at $T \rightarrow T_\Phi$, at Y values even further from [+]/[−] = 1.[19,43]

Aggregation and coacervation far from bulk stoichiometry (here deficient in micelle charge or [+]/[−] > 1) can be explained in terms of Zhang and Shklovskii's models of disproportionation.[61] Taking as an example DNA and spermine, Zhang and Shklovskii predict the formation of "condensates" (a new phase) at [+]/[−] ≠ 1, in two ways. When the host polyanion DNA is in excess, neutral complexes can form by transfer of spermine among complexes to form neutral ones, the unfavorable entropy of this disproportionation being recovered in the favorable "condensation" step. In contrast to this *inter*complex disproportionation, *intra*polyanion transfer of spermine forms a neutral end of the complex, with an un-neutralized tail. Attractive forces then take place among the neutral heads of these "tadpoles" which do not repel each other. *Inter*complex disproportionation ties phase separation to the formation of supernatant further from neutrality than the original system or to the "splitting" of aggregates into larger and more neutral species plus smaller and more highly charged species.[43] *Intra*complex disproportionation can lead to heterogeneity *within* the dense phase due to clustering of "tadpoles". In the current system, PE and micelle play the roles assigned by Zhang and Shklovskii to DNA and spermine, respectively, with exchange of micelles neutralizing some complexes and increasing [+]/[−] for others. The presence of 20 nm complexes in equilibrium with 100 nm aggregates is best explained by intercomplex disproportionation leading to more neutral complexes that are able to undergo aggregation with an increase in mass of more than an order of magnitude. For a system at larger charge excess ([+]/[−] = 1.5 *vs.* 1.37 here), more micelle transfer was needed to form aggregates, with the expulsion of smaller complexes observed as an entropy-driven "splitting" upon heating of the ambient aggregates.[43] Finally, disproportionation can occur at the micelle level, in which the distribution of micelle heterogeneity (distribution of individual micelle y) gets broadened,

Table 1 Fitting parameters obtained by the Beaucage model and the data of Fig. 6

T	$q < 0.05$	Mass fractal	$q > 0.05$	Surface fractal				
(°C)	R_g (nm)	Porod	R_g (nm)	Porod	B1 (cm^{-1} sr^{-1})	G1 (cm^{-1} sr^{-1})	B2 (cm^{-1} sr^{-1})	G2 (cm^{-1} sr^{-1})
18	41	2.0	3.0	5.0	2.4×10^{-3}	210	5.6×10^{-6}	5.76
21	49	2.1	4.0	4.8	2.6×10^{-3}	722	4.2×10^{-5}	52.8
23	43	2.1	4.0	4.8	3.9×10^{-3}	457	1.8×10^{-5}	12.5
25	33	2.3	3.4	4.9	1.0×10^{-3}	135	4.6×10^{-6}	4.65

with micelles of larger y migrating to form more nearly neutral complexes, without change in the number of micelles bound. Such intermicellar disproportionation was invoked in ref. 62 to explain the role of oppositely charged surfactants in a system where intermacromolecular aggregates and single macromolecules of copolymers coexist.

The coacervate phase

The linearity and extrapolation to zero in the plots of (Γ) *vs.* q^2 for the fast and intermediate modes F1 and F2 (Fig. 4a) demonstrated purely diffusive behaviour. The corresponding diffusion coefficients lead to $R_H = 8$ nm and 17, in agreement with previous assignments to micelles and intrapolymer soluble complexes. These are also identical to values seen in the one-phase system.[19] No temperature dependence is seen with the exception of F2 above T'_Φ, beyond which the diminution in diffusivity of F2 indicates growth of soluble complexes. These results indicate that micelles and soluble complexes can move in an unobstructed way in some region of low viscosity within the coacervate.

In contrast to F1 and F2, the existence of different slopes at low and high q regions for F3 in Fig. 4b, regardless of temperature, suggests different behavior at different length scales which can be attributed to separate events. In the low q regime, the linear dependence and zero intercept of Γ *versus* q^2 shows diffusive behavior with apparent sizes of $100 < R_H < 250$ nm. From Fig. 6, this mode can be identified with clusters of soluble aggregates (clusters of intrapolymer complexes) with $R_H^{app} \sim$100–250 nm. In contrast to the low q regime, the scattering at large q is only weakly dependent on angle (Fig. 4b) suggesting the existence of non-diffusional behavior at small length scales, along with the diffusional mode at large length scales. The results in Fig. 5 show the same q^3 dependence found by Wu *et al.*[58,59] in *e.g.* microgel particles, suggesting that this can be attributed to internal motions at small length scales within larger particles, whose diffusive behavior at large length scales is seen at low q in Fig. 4b, with an abrupt transition to smaller diffusivity at $T \rightarrow T'_\Phi$. These internal motions could arise from the disintegration and reformation of the dense domains in the coacervate, involving for example exchange of polyelectrolytes and counterions with the dilute domains, as will be discussed below. In summary, DLS results for the coacervate appear to arise from three effects: (1) translational diffusion of free micelles and intrapolymer complexes similar to those seen prior to coacervation; (2) translational diffusion of multipolymer clusters of size similar to the larger soluble aggregates seen prior to coacervation; and (3) disintegration and reformation on time scales of several ms within dense domains and reformation on time scales of several ms.

SANS data in Fig. 8 are limited to <200 nm, corresponding to micelles, intrapolymer soluble complexes and the low end of soluble aggregates, the last two not well-resolved and giving rise to an average $R_g \sim 50$ nm (Table 1). The presence of larger species is suggested by the absence of a decrease in curvature at $q < 0.003$ nm^{-1} (length scale larger than 200 nm). The mass fractal dimension increases from 2.1 to 2.3 at $T > 23$ °C along with a significant decrease in R_g, about 2 °C above the temperature at which diffusivity for F3 drops abruptly (Fig. 4b), and ~1 °C below T'_Φ (Fig. 3). SANS and DLS are consistent with an increase in the size of soluble aggregates during the approach to T'_Φ, followed by their collapse at $T < T'_\Phi$.

Cryo-TEM

DLS and SANS results indicate both diffusive and nondiffusive motion at multiple length scales, preservation of rapid micelle diffusion at all conditions, and compaction of dense domains with increasing temperature. Somewhat counter-intuitively, DLS indicated non-diffusive motion at small length scales and diffusive motions at large length scales. Further insights into these phenomena are provided by the Cryo-TEM image of the coacervate in Fig. 9, which shows interconnected roughly 200 nm clusters separated by dilute (micelle-deficient) domains, such features of coacervate mesophases were observed also by other techniques applied to both polyelectrolyte–micelle and polyelectrolyte–protein systems.[35,46] Diffusive modes arise in both dilute and dense domains. Polymer-bound micelles in the dilute domains appear primarily as concatenated *ca.* 10 nm dots. These polyelectrolyte–micelle necklaces[63] are in equilibrium with highly diffusive free micelles that are readily observed by DLS but cannot be distinguished in the Cryo-TEM due to low contrast. While diffusional modes of the polyelectrolyte in dilute domains are not directly observable by DLS or SANS, the evidence for both transfer of polycations from dense to dilute domains, and for the relatively free diffusive motions of those polymers has been found by PFGNMR spectra of coacervates formed from PDADMAC with proteins in place of micelles.[7] Tightly packed micelle-decorated chains are most obvious within the 100–300 nm clusters that are separated by regions of somewhat lower density. The clusters themselves are responsible for the apparent increase in neutron scattering at the low-q end of the SANS spectra in Fig. 8, and for the slow diffusive component of F3 seen by DLS.

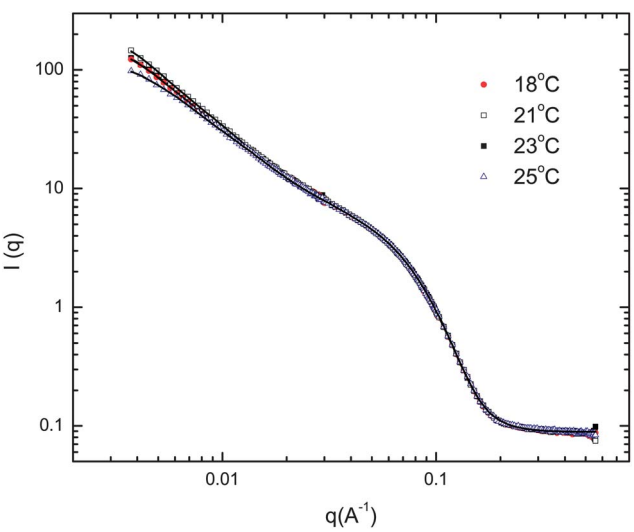

Fig. 8 SANS profiles for the coacervate of PDADMAC/TX100-SDS at different temperatures.

Their apparent hydrodynamic radii of 100–250 nm can be attributed to the exchange between dense and dilute domains of the clusters which are constrained by labile interconnections but nonetheless appears diffusive because of the short lifetime of interconnections. The disentanglements of the interconnections do not of themselves produce any translation or any change in scattering; their only effect is to allow diffusion within dense domains. Dense polyelectrolyte–colloid domains have also been observed for polyelectrolyte–protein coacervates by Cryo-TEM[34] where their translocation leads to a slow diffusive mode.[36] For such coacervates, two modes of diffusion for a non-interacting (Ficoll) probe, were obtained by FRAP and were attributed to viscous domains of high protein concentration embedded in a continuous more dilute phase,[35] analogous to the micelle-poor regions of Fig. 9.

Dynamics of intra-coacervate dense domains

Non-diffusive scattering modes arise from the disintegration of dense domains due to both labile interconnections among clusters, and intra-cluster rearrangements. Dense domain lifetimes are reflected in viscoelastic behavior for both polyelectrolyte–micelle and polyelectrolyte–protein coacervates. We propose intra-cluster rearrangements involving micelle motions and concomitant disentanglement of polymer chains. These lead to the non-diffusive mode (Fig. 4b) with a relaxation time $\tau \cong 2$ ms obtained by fitting DLS spectra to a stretched exponential (not shown). Further evidence for the identification of this relaxation comes from the 50% decrease in Γ from the high q data in Fig. 4b as the temperature increases from 12 to 21 °C, prior to phase separation at $T'_{\Phi} = 24$ °C. This is supported by visual observations of temperature-induced syneresis consistent with increasing desolvation of the dense phase slowing down all intra-cluster processes.[46] In polyelectrolyte–protein coacervates non-diffusive slow modes also appear, but are well-resolved from diffusive slow modes.[34] In that system it is possible to confirm by PFGNMR that these non-diffusive modes are actually fast compared to the 30–100 ms required for disintegration of clusters.[7] Changes in inter-cluster connectivity in and of itself do not lead to measurable scattering fluctuations, but are best evidenced by rheology. For polyelectrolyte–protein coacervates, time-dependent measurements of the moduli were performed after extensive preshear; G' values decreased markedly and slowly recovered initial values owing to the existence of interconnected dense domains.[34]

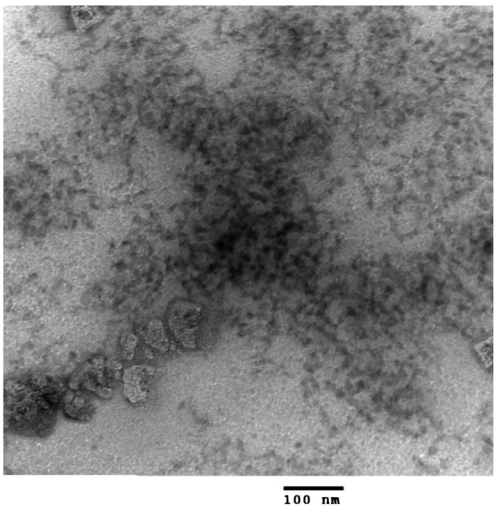

Fig. 9 Cryo-TEM image the coacervate of PDADMAC/TX100-SDS.

Comparison with models

Complex disproportionation. Certain key aspects of the image of Fig. 9 can be understood in terms of the theoretical model for phase separation ("condensation") from solutions of oppositely charge macroions by Shklovskii and Zhang.[61] As discussed above in the context of the approach to coacervation, this model accounts for phase separation away from net charge stoichiometry through a disproportionation process that provides correlation energy for the interactions of polyelectrolyte–colloid aggregates. This results in a dilute phase further removed from charge neutrality than the initial solution, and a dense phase with [+]/[−] closer to unity. In addition to the enthalpic attractions between quasi-neutral aggregates, the principal role of entropy in coacervation, mainly arises from expulsion of small ions[19] into the dilute phase and from an increase in chain configurational entropy,[1] not considered in Shklovskii *et al.* Very similar effects can be invoked to account for structural features in Fig. 9, but here acting on a microscopic scale. First, the *ca.* 200 nm micelle-rich regions, too small to exhibit dense–dilute domain interfaces, must contain some polymer chains that extend into the more dilute regions. Relatively micelle-rich regions of these chains, formed by *intra*-polymer disproportionation, attain a level of neutrality allowing them to cluster together at the 100–300 nm length scale. In dilute regions, the extruded polycations are evidently micelle-bound to a considerable degree, and their large persistence length (*ca.* 25 nm obtained applying ImageJ (ref. 64) to Fig. 9), suggests that the micelles stiffen the PE to which they are bound. The polymer chains in the dilute regions are nevertheless depleted in micelle charge relative to the dense domains, and so must be neutralized by Cl^-. This release of the counterions and excess polycation into dilute regions is the exact counterpart of events during the initial coacervation, but on a microscopic scale. The fact that neither of the two microdomains is electrically neutral limits the length scale of the structures in Fig. 9. Consequently, it can be expected that the size of the intra-coacervate dense domains will decrease as [+]/[−] departs from unity. On the other hand, an increase in the volumes of intra-coacervate dilute domains available to counterions is entropically favorable, and should therefore be subject to an effect of temperature. The change in the volume available to polymer chains, is however insufficient to lead to the gain in configurational entropy, expected for the initial coacervation.

Core–corona model

Gummel *et al.* have described a related system formed from lysozyme and excess polystyrenesulfonate (PSS) although the

phase of the dense insoluble product is not precisely defined.[40] This description is deduced from SANS results for a system that differs from ours in that the interaction between PSS and fully charged lysozyme is stronger in pure water. Like Shklovskii's model, the description of Gummel *et al.* also accounts for phase separation far from charge stoichiometry but unlike Shklovskii *et al.*, it includes counterion release. In fact, the distribution of counterions obtained by contrast matching provides a rather precise picture of the probable distribution of macroions. Gummel *et al.* explain how the initial aggregates rearrange to form neutral domains (protein-rich "cores") surrounded by polyanion-rich "coronas." The polyelectrolyte–protein complexes are dense and collapsed and retain few counterions, in contrast to the complexes formed in the present work at relatively low micelle charge and high salt. For this reason, micelle–polycation dense domains here are more dynamic, heterogeneous and interconnected, while the dilute domains include both the colloid and the excess polymer and its counterions. The *ca.* 200 nm objects in Fig. 9 are relatively amorphous and transient analogs of the more solid-like and permanent polyelectrolyte–protein "cores" of ref. 40. The dense–dilute interface is also diffuse and transient. The connectivity among the dense domains through their 300–500 nm spacing is manifested in the viscoelastic behavior,[34] and the dynamics of probe diffusion observed in fluorescence recovery after photobleaching.[35]

Soft colloids

We designated as the "colloid model" of coacervation a process wherein "soft" colloidal particles undergo liquid–liquid phase separation at a critical volume fraction dependent on interparticle interactions. While examination of the coacervate does reveal objects with sizes similar to species in solution – micelles, intrapolymer complexes and interpolymer complex – we conclude for a number of reasons that the interactions that give rise to coacervation are much more nuanced than the interparticle forces in the "colloid model". First, substantial rearrangements of particles take place prior to liquid–liquid phase separation, including exchange of their constituent micelles. The requisite energy compensated for by the favorable energy of phase separation. This energy, primarily comprising entropic gains in configurational energy of polymers and release of counterions, is entirely consistent with the absence of measurable enthalpies of coacervation; and describing it as an interparticle interaction would be overly reductionist. Second, the combination pre-coacervate obects can be regarded in terms of the elimination of a surface tension instead of conglomeration of aggregation. Third, instead of a critical volume fraction for coacervation, we observe that coacervation cannot be reversed by dilution and that coacervation in fact appears to be subject to self-suppression.[42,43] Finally, the appearance of objects within the coacervate with sizes comparable to soluble complexes and soluble aggregates arises from similar enthalpic and entropic forces operating in both phases, and not from the actual incorporation of those complexes in the dense phase.

Driving forces for intracoacervate mesophase separation

The mesophase structure of coacervates arises from the combination of a short-range attraction with a long-range repulsive force present when [+]/[−] is different than unity, and leading to forms of disproportionation in the coacervate. Disproportionation, primarily *inter*polymer in the one-phase state, can be visualized as a transient *intra*polymer rearrangement in the formation of coacervate. This structural rearrangement in the coacervate suggests our system exhibits the features of model 2, which include the compositional difference between supernatant and coacervate, even if the clusters within these two phases might be of comparable size. A similar combination of short-range attraction and long-range repulsion forces in both supernatant and coacervate might be responsible for the similar sizes in two phases since short-range attractions stabilize dense domains while long-range repulsions dictate the length scale of their interconnection.[34]

Conclusions

Polyelectrolyte–micelle systems in solution and in coacervate comprise free micelles, soluble complexes, and soluble aggregates that form a hierarchy of equilibrium structures. These structures arise from primary complexes that interact with each other through short-range attraction and long-range repulsion; the balance of these forces determines the length scales of self-assembly in both phases. In solution, the association of soluble aggregates is opposed by charge accumulation and is promoted by the enhancement of ion-pairing and counterion release, and may be viewed as a reduction of surface free energy. Charge neutralization in solutions with charge stoichiometry ([+]/[−] > 1) can be achieved by the expulsion of excess polycation to either the periphery of the soluble aggregate or to other complexes (disproportionation). In the coacervate, similar disproportionation leads to expulsion of excess polycations and their counterions to 50–300 nm dilute domains. This process leads to the creation of proximal regions of more complete ion-pairing (charge neutralization) and higher density in both solution and coacervate; these serve as transient crosslinks in the viscoelastic coacervate. The driving forces for formation of near-neutral aggregates in solution and analogous dense domains in the coacervate are the enthalpy of interacting complementary charges, the concomitant entropy of counterion release, and the increase in configurational chain entropy. Structural similarities between the soluble aggregates and coacervate dense domains thus arise from similar balances of enthalpic and entropic forces.

Acknowledgements

Acknowledgement is made to the donors of The American Chemical Society Petroleum Research Fund for partial support of this research. Support from the National Science Foundation (NSF) (Grant CBET-0966923 and DMR-0907195) is acknowledged. This work utilized neutron research facilities supported in part by the National Science Foundation under Agreement no. DMR-0454672 and by the National Institute of Standards

and Technology, U. S. Department of Commerce. We also thank Dr JoAn Hudson (Clemson University) for assistance with Cryo-TEM; Dr Yun Liu, Dr David F. R. Mildner, and Dr Boualem Hammouda (NIST, Gaithersburg, MD) for assistance with SANS; and also Prof. Surita Bhatia (Stony Brook University) for assistance with SANS data analysis.

References

1 A. Veis and C. Aranyi, *J. Phys. Chem.*, 1960, **64**, 1203–1210.
2 S. S. Singh, A. K. Siddhanta, R. Meena, K. Prasad, S. Bandyopadhyay and H. B. Bohidar, *Int. J. Biol. Macromol.*, 2007, **41**, 185–192.
3 R. Chollakup, W. Smitthipong, C. D. Eisenbach and M. Tirrell, *Macromolecules*, 2010, **43**, 2518–2528.
4 E. Spruijt, A. H. Westphal, J. W. Borst, M. A. C. Stuart and J. van der Gucht, *Macromolecules*, 2010, **43**, 6476–6484.
5 B. Mohanty, V. K. Aswal, P. S. Goyal and H. B. Bohidar, *Pramana – Journal of Physics*, 2004, **63**, 271–276.
6 A. Srivastava, J. H. Waite, G. D. Stucky and A. Mikhailovsky, *Macromolecules*, 2009, **42**, 2168–2176.
7 A. R. Menjoge, A. B. Kayitmazer, P. L. Dubin, W. Jaeger and S. Vasenkov, *J. Phys. Chem. B*, 2008, **112**, 4961–4966.
8 S. L. Turgeon, M. Beaulieu, C. Schmitt and C. Sanchez, *Curr. Opin. Colloid Interface Sci.*, 2003, **8**, 401–414.
9 C. Schmitt and S. L. Turgeon, *Adv. Colloid Interface Sci.*, 2011, **167**, 63–70.
10 D. S. Hwang, H. B. Zeng, A. Srivastava, D. V. Krogstad, M. Tirrell, J. N. Israelachvili and J. H. Waite, *Soft Matter*, 2010, **6**, 3232–3236.
11 R. J. Stewart, C. S. Wamg and H. Shao, *Adv. Colloid Interface Sci.*, 2011, **167**, 85–93.
12 C. Schmitt, C. Sanchez, S. Desobry-Banon and J. Hardy, *Crit. Rev. Food Sci. Nutr.*, 1998, **38**, 689–753.
13 E. Kizilay, A. B. Kayitmazer and P. L. Dubin, *Adv. Colloid Interface Sci.*, 2011, **167**, 24–37.
14 D. C. Li, M. S. Kelkar and N. J. Wagner, *Langmuir*, 2012, **28**, 10348–10362.
15 Y. G. Mishael and P. L. Dubin, *Environ. Sci. Technol.*, 2005, **39**, 8475–8480.
16 J. L. Xia, K. Mattison, V. Romano, P. L. Dubin and B. B. Muhoberac, *Biopolymers*, 1997, **41**, 359–365.
17 A. C. Lee and Y. H. Hong, *Food Res. Int.*, 2009, **42**, 733–738.
18 C. Sanchez, G. Mekhloufi, C. Schmitt, D. Renard, P. Robert, C. M. Lehr, A. Lamprecht and J. Hardy, *Langmuir*, 2002, **18**, 10323–10333.
19 A. Kumar, P. L. Dubin, M. J. Hernon, Y. J. Li and W. Jaeger, *J. Phys. Chem. B*, 2007, **111**, 8468–8476.
20 C. B. Bucur, Z. Sui and J. B. Schlenoff, *J. Am. Chem. Soc.*, 2006, **128**, 13690–13691.
21 D. Priftis, N. Laugel and M. Tirrell, *Langmuir*, 2012, **28**, 15947.
22 P. M. Biesheuvel and M. A. C. Stuart, *Langmuir*, 2004, **20**, 2785–2791.
23 J. van der Gucht, E. Spruijt, M. Lemmers and M. A. C. Stuart, *J. Colloid Interface Sci.*, 2011, **361**, 407–422.
24 A. Veis, *Adv. Colloid Interface Sci.*, 2011, **167**, 2–11.
25 I. Michaeli, J. T. G. Overbeek and M. J. Voorn, *J. Polym. Sci.*, 1957, **23**, 443–450.
26 J. Lee, Y. O. Popov and G. H. Fredrickson, *J. Chem. Phys.*, 2008, **128**, 224908.
27 Y. Wang, J. Y. Gao and P. L. Dubin, *Biotechnol. Prog.*, 1996, **12**, 356–362.
28 J. Xia, H. Zhang, D. R. Rigsbee, P. L. Dubin and T. Shaikh, *Macromolecules*, 1993, **26**, 2759–2766.
29 J. Xia, P. L. Dubin and H. Dautzenberg, *Langmuir*, 1993, **9**, 2015–2019.
30 Y. L. Wang, K. Kimura, Q. R. Huang, P. L. Dubin and W. Jaeger, *Macromolecules*, 1999, **32**, 7128–7134.
31 X. Y. Wang, Y. Q. Li, Y. W. Wang, J. Lal and Q. R. Huang, *J. Phys. Chem. B*, 2007, **111**, 515–520.
32 F. Weinbreck, H. S. Rollema, R. H. Tromp and C. G. de Kruif, *Langmuir*, 2004, **20**, 6389–6395.
33 S. Chodankar, V. K. Aswal, J. Kohlbrecher, R. Vavrin and A. G. Wagh, *Phys. Rev. E: Stat., Nonlinear, Soft Matter Phys.*, 2008, **78**, 031913.
34 A. B. Kayitmazer, S. P. Strand, C. Tribet, W. Jaeger and P. L. Dubin, *Biomacromolecules*, 2007, **8**, 3568–3577.
35 A. B. Kayitmazer, H. B. Bohidar, K. W. Mattison, A. Bose, J. Sarkar, A. Hashidzume, P. S. Russo, W. Jaeger and P. L. Dubin, *Soft Matter*, 2007, **3**, 1064–1076.
36 H. Bohidar, P. L. Dubin, P. R. Majhi, C. Tribet and W. Jaeger, *Biomacromolecules*, 2005, **6**, 1573–1585.
37 F. Cousin, J. Gummel, D. Clemens, I. Grillo and F. Boue, *Langmuir*, 2010, **26**, 7078–7085.
38 F. Cousin, J. Gummel, S. Combet and F. Boue, *Adv. Colloid Interface Sci.*, 2011, **167**, 71–84.
39 A. Stradner, H. Sedgwick, F. Cardinaux, W. C. K. Poon, S. U. Egelhaaf and P. Schurtenberger, *Nature*, 2004, **432**, 492–495.
40 J. Gummel, F. Cousin and F. Boue, *J. Am. Chem. Soc.*, 2007, **129**, 5806–5807.
41 D. R. Rigsbee and P. L. Dubin, *Langmuir*, 1996, **12**, 1928–1929.
42 Y. Li, P. L. Dubin, H. Dautzenberg, U. Luck, J. Hartmann and Z. Tuzar, *Macromolecules*, 1995, **28**, 6795–6798.
43 E. Kizilay, S. Maccarrone, E. Foun, A. D. Dinsmore and P. L. Dubin, *J. Phys. Chem. B*, 2011, **115**, 7256–7263.
44 W. C. K. Poon, *J. Phys.: Condens. Matter*, 2002, **14**, R859–R880.
45 P. J. Flory, *J. Chem. Phys.*, 1944, **12**, 114–115.
46 P. L. Dubin, Y. J. Li and W. Jaeger, *Langmuir*, 2008, **24**, 4544–4549.
47 M. W. Liberatore, N. B. Wyatt, M. Henry, P. L. Dubin and E. Foun, *Langmuir*, 2009, **25**, 13376–13383.
48 F. W. Wiegel, *J. Phys. A: Math. Gen.*, 1977, **10**, 299.
49 M. Muthukumar, *J. Chem. Phys.*, 1987, **86**, 7230.
50 J. Janiak, L. Piculell, G. Olofsson and K. Schillén, *Phys. Chem. Chem. Phys.*, 2011, **13**, 3126–3138.
51 K. Thalberg, B. Lindman and G. Karlstromt, *J. Phys. Chem.*, 1991, **95**, 6004–6011.
52 J. Groenewold and W. K. Kegel, *J. Phys. Chem. B*, 2001, **105**, 11702–11709.

53 B. Zhang, G. F. Kirton and P. L. Dubin, *Abstr. Pap., Jt. Conf. – Chem. Inst. Can. Am. Chem. Soc.*, 2001, **222**, U324.
54 M. Hahn and W. Jaeger, *Angew. Makromol. Chem.*, 1992, **198**, 165–178.
55 S. W. Provencher, *Comput. Phys. Commun.*, 1982, **27**, 229–242.
56 S. R. Kline, *J. Appl. Crystallogr.*, 2006, **39**, 895–900.
57 G. Beaucage, *J. Appl. Crystallogr.*, 1995, **28**, 717–728.
58 C. Wu, K. K. Chan and K. Q. Xia, *Macromolecules*, 1995, **28**, 1032–1037.
59 C. Wu and S. Q. Zhou, *Macromolecules*, 1996, **29**, 1574–1578.
60 K. Kogej, *Adv. Colloid Interface Sci.*, 2010, **158**, 68–83.
61 R. Zhang and B. T. Shklovskii, *Physica A*, 2005, **352**, 216–238.
62 E. E. Makhaeva, H. Tenhu and A. R. Khokhlov, *Macromolecules*, 2002, **35**, 1870–1876.
63 L. T. Lee and B. Cabane, *Macromolecules*, 1997, **30**, 6559–6566.
64 M. D. Abràmoff, P. J. Magalhães and S. J. Ram, *Biophotonics International*, 2004, **11**, 36–42.

